

Narrowband and broadband active control in an enclosure using the acoustic energy density

John W. Parkins

RTH Systems, 135 Storm Road, Groton, New York 13073

Scott D. Sommerfeldt

Department of Physics, Brigham Young University, N241 ESC, Provo, Utah 84602

Jiri Tichy

Acoustics Department, The Pennsylvania State University, Applied Science Building, North Atherton Street, State College, Pennsylvania 16802

(Received 29 July 1999; accepted for publication 28 March 2000)

An active control system based on the acoustic energy density is investigated. The system is targeted for use in three-dimensional enclosures, such as aircraft cabins and rooms. The acoustic energy density control method senses both the potential and kinetic energy densities, while the most popular control systems of the past have relied on the potential energy density alone. Energy density fields are more uniform than squared pressure fields, and therefore, energy density measurements are less sensitive to sensor location. Experimental results are compared to computer-generated results for control systems based on energy density and squared pressure for a rectangular enclosure measuring $1.5 \times 2.4 \times 1.9$ m. Broadband and narrowband frequency pressure fields in the room are controlled experimentally. Pressure-field and mode-amplitude data are presented for the narrowband experiments, while spectra and pressure-field data are presented for the broadband experiment. It is found that the energy density control system has superior performance to the squared pressure control system since the energy density measurement is more capable of observing the modes of a pressure field. Up to 14.4 and 3.8 dB of cancellation are achieved for the energy density control method for the narrowband and broadband experiments presented, respectively. © 2000 Acoustical Society of America. [S0001-4966(00)02007-5]

PACS numbers: 43.50.Ki [MRS]

INTRODUCTION

Most active control systems for use in three-dimensional enclosures employ pressure microphones as error sensors. These control systems typically minimize the sum of the squared pressures at the microphone locations, effectively minimizing the sum of the potential energy densities at these points.¹ However, acoustic energy exists in two states: potential energy in the form of pressure, and kinetic energy in the form of particle velocity. Systems based on minimizing potential energy density are therefore neglecting half the acoustic energy. Reduction of the potential energy density at a point in space may significantly increase both the kinetic energy density at that point as well as the total energy in the enclosure. A control system based on minimizing the sum of the total energy densities at discrete points yields improved global noise reduction, since it attenuates both forms of acoustic energy.

Since the early 1990s, active control systems based on energy density have been investigated. In 1992, Sommerfeldt and Nashif studied the efficacy of a single-axis energy density based system for use in ducts.² In 1995, Sommerfeldt *et al.* investigated a three-axis energy density control system, using a single sensor, for use in rectangular enclosures.³ Park and Sommerfeldt modeled broadband active control in a one-dimensional enclosure in 1995.⁴ Recently, Qiu *et al.* presented a theoretical comparison of near-field error sensor control systems which included energy density sensing.⁵

The previous work in energy density-based active control systems is expanded in this paper to include narrowband control using three-axis energy density sensing with multiple sensors/control sources, and broadband control using a single energy density sensor/control source, in a rectangular enclosure. In analyzing the effectiveness of the energy density control strategy, the performance is compared to the more common system based on minimizing the sum of the squared pressures. A computer model is used to predict the results of active cancellation for both strategies for active control, as well as modeling a method whereby the integrated potential energy density over the enclosure volume is minimized. The latter system has been proposed as an optimal control system.⁶ Experimental results are presented for the energy density and squared pressure control schemes. Pressure-field as well as mode-amplitude data are presented for both computer-generated and experimental data.

I. THE ACOUSTIC ENERGY DENSITY

The time-averaged total acoustic energy density at a point in space, $\mathbf{x} = (x, y, z)$, is defined as

$$e(\mathbf{x}) \equiv U(\mathbf{x}) + T(\mathbf{x}), \quad (1)$$

which is the sum of the potential energy density, $U(\mathbf{x})$, and the kinetic energy density, $T(\mathbf{x})$. The potential energy is stored in the form of pressure, while the kinetic energy is manifested as particle velocity. In terms of the acoustic pres-

sure and particle velocity, the total energy density can be written as

$$e(\mathbf{x}) = \frac{1}{4\rho c^2} |\hat{p}(\mathbf{x})|^2 + \frac{\rho}{4} |\hat{\mathbf{v}}(\mathbf{x})|^2, \quad (2)$$

where $\hat{\mathbf{v}}(\mathbf{x}) = (\hat{v}_x(\mathbf{x}), \hat{v}_y(\mathbf{x}), \hat{v}_z(\mathbf{x}))$ is the vector particle velocity, c is the speed of sound, and ρ is the density. Equation (2) can also be written as

$$e(\mathbf{x}) = \frac{1}{4\rho c^2} |\hat{p}(\mathbf{x})|^2 + \frac{\rho}{4} |\hat{v}_x(\mathbf{x})|^2 + \frac{\rho}{4} |\hat{v}_y(\mathbf{x})|^2 + \frac{\rho}{4} |\hat{v}_z(\mathbf{x})|^2. \quad (3)$$

Hence, four scalar acoustic quantities are needed to determine the acoustic energy density at a point in space.

II. MODAL REPRESENTATION OF THE PRESSURE FIELD

The complex pressure $\hat{p}(\mathbf{x})$ in an enclosure can be represented by an infinite sum of the weighted eigenfunctions of the enclosure as

$$\hat{p}(\mathbf{x}) = \sum_{N=1}^{\infty} \hat{A}_N \Psi_N(\mathbf{x}). \quad (4)$$

The eigenfunctions or mode functions, $\Psi_N(\mathbf{x})$, for a rigid undamped rectangular room with dimensions $L_x \times L_y \times L_z$ are

$$\Psi_N(\mathbf{x}) = \cos k_x x \cos k_y y \cos k_z z, \quad (5)$$

where

$$k_x = \frac{l\pi}{L_x}, \quad k_y = \frac{m\pi}{L_y}, \quad \text{and} \quad k_z = \frac{n\pi}{L_z}. \quad (6)$$

The mode indices l , m , and n each take on integer values. The resonance frequencies, f_N , of the enclosure are given by

$$f_N = \frac{c}{2\pi} \sqrt{k_x^2 + k_y^2 + k_z^2} = \frac{ck}{2\pi}, \quad (7)$$

where k is the acoustic wave number. If a point monopole source is added to the enclosure to control the field, the complex pressure can be represented by

$$\hat{p}(\mathbf{x}) = \sum_{N=1}^{\infty} (\hat{A}_N + \hat{B}_N \hat{Q}_c) \Psi_N(\mathbf{x}), \quad (8)$$

where \hat{Q}_c is the complex source strength of the monopole. If G monopole sources are used to control the field, the complex pressure field can be written as

$$\hat{p}(\mathbf{x}) = \sum_{N=1}^{\infty} \left(\hat{A}_N + \sum_{g=1}^G \hat{B}_{N,g} \hat{Q}_{c,g} \right) \Psi_N(\mathbf{x}). \quad (9)$$

Equation (9) can also be written as

$$\hat{p}(\mathbf{x}) = \sum_{N=1}^{\infty} \hat{C}_N \Psi_N(\mathbf{x}), \quad (10)$$

where $\hat{C}_N = \hat{A}_N + \sum_{g=1}^G \hat{B}_{N,g} \hat{Q}_{c,g}$ are the complex modal amplitudes of the resulting pressure field.

III. OPTIMAL CONTROL SOLUTIONS

The performance functions for minimizing the integrated potential energy, squared pressure, and energy density can be expressed as

$$J_{PE} = \int_V \frac{|\hat{p}(\mathbf{x})|^2}{4\rho c^2} dV, \quad (11a)$$

$$J_{SP} = \sum_{i=1}^I |\hat{p}(\mathbf{x}_i)|^2, \quad (11b)$$

$$J_{ED} = \sum_{i=1}^I \frac{1}{4\rho c^2} |\hat{p}(\mathbf{x}_i)|^2 + \frac{\rho}{4} |\hat{\mathbf{v}}(\mathbf{x}_i)|^2, \quad (11c)$$

where there are I sensors, located at the positions \mathbf{x}_i .

Using Eq. (9), and minimizing Eq. (11a) with respect to the G control source strengths, $\hat{Q}_{c,g}$, yields the optimal source strengths for the integrated potential energy density control strategy. These optimal source strengths are given by

$$\hat{Q}_{c,PE} = -(\hat{\mathbf{B}}'^H \hat{\mathbf{B}}')^{-1} \hat{\mathbf{B}}'^H \hat{\mathbf{A}}', \quad (12)$$

where

$$\hat{\mathbf{A}}' \equiv [\hat{A}'_1 \quad \cdots \quad \hat{A}'_N \quad \cdots \quad \hat{A}'_{\infty}]^T, \quad (13)$$

$$\hat{\mathbf{B}}' \equiv \begin{bmatrix} \hat{B}'_{1,1} & \cdots & \hat{B}'_{N,1} & \cdots & \hat{B}'_{\infty,1} \\ \vdots & \ddots & \vdots & \ddots & \vdots \\ \hat{B}'_{1,g} & \cdots & \hat{B}'_{N,g} & \cdots & \hat{B}'_{\infty,g} \\ \vdots & \ddots & \vdots & \ddots & \vdots \\ \hat{B}'_{1,G} & \cdots & \hat{B}'_{N,G} & \cdots & \hat{B}'_{\infty,G} \end{bmatrix}, \quad (14)$$

and

$$\hat{Q}_{c,PE} \equiv [\hat{Q}_{c,1}, \dots, \hat{Q}_{c,g}, \dots, \hat{Q}_{c,G}]^T. \quad (15)$$

The elements of $\hat{\mathbf{A}}'$ are related to \hat{A}_N by $\hat{A}'_N = \hat{A}_N \sqrt{V \Lambda_N}$, while the elements of $\hat{\mathbf{B}}'$ are related to $\hat{B}_{N,g}$ by $\hat{B}'_{N,g} = \hat{B}_{N,g} \sqrt{V \Lambda_N}$. The Hermitian transpose is indicated by a superscript H . A single solution exists if the number of control sensors is greater than or equal to the number of control sources. For the special case of a single control source, the complex amplitude of the control source is

$$\hat{Q}_{c,PE} = -\frac{\sum_{N=1}^{\infty} \hat{A}_N \hat{B}_N^* \Lambda_N}{\sum_{N=1}^{\infty} \hat{B}_N \hat{B}_N^* \Lambda_N}, \quad (16)$$

where

$$\Lambda_N = \frac{1}{\epsilon_l \epsilon_m \epsilon_n} \quad (17)$$

and

$$\epsilon_i = \begin{cases} 1, & \text{if } i=0 \\ 2, & \text{if } i \neq 0. \end{cases} \quad (18)$$

Minimizing Eq. (11b) with respect to the G control source strengths, $\hat{Q}_{c,g}$, yields the optimal source strengths for a control system based on the squared pressure. These source strengths are given by

$$\hat{Q}_{c,SP} = \hat{C}^{-1} \hat{D}, \quad (19)$$

where

$$\hat{Q}_{c,SP} = \begin{bmatrix} \Re\{Q_{c,1}\} \\ \Im\{Q_{c,1}\} \\ \Re\{Q_{c,2}\} \\ \Im\{Q_{c,2}\} \\ \vdots \\ \Re\{Q_{c,G}\} \\ \Im\{Q_{c,G}\} \end{bmatrix}, \quad (20)$$

$$\hat{D} = \begin{bmatrix} -\sum_{i=1}^I \sum_{N=1}^{\infty} \sum_{M=1}^{\infty} \Re\{\hat{B}_{N,1}^* \hat{A}_M\} \Psi_N(\mathbf{x}_i) \Psi_M(\mathbf{x}_i) \\ \vdots \\ -\sum_{i=1}^I \sum_{N=1}^{\infty} \sum_{M=1}^{\infty} \Re\{\hat{B}_{N,G}^* \hat{A}_M\} \Psi_N(\mathbf{x}_i) \Psi_M(\mathbf{x}_i) \\ -\sum_{i=1}^I \sum_{N=1}^{\infty} \sum_{M=1}^{\infty} \Im\{\hat{B}_{N,1}^* \hat{A}_M\} \Psi_N(\mathbf{x}_i) \Psi_M(\mathbf{x}_i) \\ \vdots \\ -\sum_{i=1}^I \sum_{N=1}^{\infty} \sum_{M=1}^{\infty} \Im\{\hat{B}_{N,G}^* \hat{A}_M\} \Psi_N(\mathbf{x}_i) \Psi_M(\mathbf{x}_i) \end{bmatrix}, \quad (21)$$

\hat{C}^{-1}

$$= \begin{bmatrix} c_{11} & c_{12} & \cdots & c_{1(2G-1)} & c_{1(2G)} \\ \vdots & & \ddots & & \vdots \\ c_{G1} & c_{G2} & \cdots & c_{G(2G-1)} & c_{G(2G)} \\ c_{(G+1)1} & c_{(G+1)2} & \cdots & c_{(G+1)(2G-1)} & c_{(G+1)(2G)} \\ \vdots & & \ddots & & \vdots \\ c_{(2G)1} & c_{(2G)2} & \cdots & c_{(2G)(2G-1)} & c_{(2G)(2G)} \end{bmatrix} \quad (22)$$

and

$$\begin{aligned} c_{p(2q-1)} &= \sum_{i=1}^I \sum_{N=1}^{\infty} \sum_{M=1}^{\infty} \Re\{\hat{B}_{N,p}^* \hat{B}_{M,q}\} \Psi_N(\mathbf{x}_i) \Psi_M(\mathbf{x}_i), \\ c_{p(2q)} &= -\sum_{i=1}^I \sum_{N=1}^{\infty} \sum_{M=1}^{\infty} \Im\{\hat{B}_{N,p}^* \hat{B}_{M,q}\} \Psi_N(\mathbf{x}_i) \Psi_M(\mathbf{x}_i), \\ c_{(G+p)(2q-1)} &= \sum_{i=1}^I \sum_{N=1}^{\infty} \sum_{M=1}^{\infty} \Im\{\hat{B}_{N,p}^* \hat{B}_{M,q}\} \Psi_N(\mathbf{x}_i) \Psi_M(\mathbf{x}_i), \\ c_{(G+p)(2q)} &= \sum_{i=1}^I \sum_{N=1}^{\infty} \sum_{M=1}^{\infty} \Re\{\hat{B}_{N,p}^* \hat{B}_{M,q}\} \Psi_N(\mathbf{x}_i) \Psi_M(\mathbf{x}_i), \end{aligned} \quad (23)$$

where p and q are integers ranging from 1 to G . Again, a single solution exists if the number of control sensors is greater than or equal to the number of control sources. For the special case of a single control source, the complex amplitude of the control source is given by

$$\hat{Q}_{c,SP} = -\frac{\sum_{i=1}^I \sum_{N=1}^{\infty} \sum_{M=1}^{\infty} \hat{A}_N \Psi_N(\mathbf{x}_i) \Psi_M(\mathbf{x}_i)}{\sum_{i=1}^I \sum_{N=1}^{\infty} \sum_{M=1}^{\infty} \hat{B}_N \Psi_N(\mathbf{x}_i) \Psi_M(\mathbf{x}_i)}. \quad (24)$$

Minimizing Eq. (11c) with respect to the G control source strengths $\hat{Q}_{c,g}$ yields the same solutions defined in Eqs. (19)–(23), where the function $\Psi_N(\mathbf{x}_i) \Psi_M(\mathbf{x}_i)$ is replaced by $F_{NM}(\mathbf{x}_i)$. These are the optimal source strengths when employing the energy density control. The function $F_{NM}(\mathbf{x}_i)$ is defined by

$$F_{NM}(\mathbf{x}_i) \equiv \Psi_N(\mathbf{x}_i) \Psi_M(\mathbf{x}_i) + \frac{\nabla \Psi_N(\mathbf{x}_i) \nabla \Psi_M(\mathbf{x}_i)}{k^2}. \quad (25)$$

For the special case of a single control source, the complex amplitude of the control source is given by

$$\hat{Q}_{c,ED} = -\frac{\sum_{i=1}^I \sum_{N=1}^{\infty} \sum_{M=1}^{\infty} \hat{A}_N F_{NM}(\mathbf{x}_i)}{\sum_{i=1}^I \sum_{N=1}^{\infty} \sum_{M=1}^{\infty} \hat{B}_N F_{NM}(\mathbf{x}_i)}. \quad (26)$$

IV. CONTROL IMPLEMENTATION

The pressure as well as the three components of vector velocity are needed to implement the energy density control, as indicated by Eq. (3). Single-element velocity sensors, such as gradient microphones, do not have the accuracy and response needed in the frequency range of interest. To determine the acoustic velocity along an axis, two pressure microphones can be used.

Euler's equation in one dimension relates the gradient of the pressure to the time derivative of the velocity at a given point through the relation

$$\rho \frac{\partial v_x(x,t)}{\partial t} = -\frac{\partial p(x,t)}{\partial x}, \quad (27)$$

which can be rewritten as

$$v_x(x,t) = -\frac{1}{\rho} \int_{-\infty}^t \frac{\partial p(x,\tau)}{\partial x} d\tau. \quad (28)$$

Equation (28) can be approximated as

$$v_x(x,t) \approx -\frac{1}{\rho} \int_{-\infty}^t \frac{p_2(\tau) - p_1(\tau)}{\Delta x} d\tau, \quad (29)$$

where $p_2(t)$ and $p_1(t)$ are the pressures measured by two microphones separated by a distance Δx .⁷ Hence, the velocity can be estimated by integrating the difference between the outputs of two pressure microphones separated in space. The integration can be performed using analog electronics, but was implemented digitally in the control processor. An inexpensive energy density sensor was developed for this project, and its characteristics are explained in a recently submitted paper.⁸ The sensor employs six electret microphones mounted on the surface of a 1-in. (0.0254-m) radius wooden sphere. The errors associated with the energy density sensor were found to be minimal (within ± 1.75 dB) for the frequencies used in the active control experiments presented here.

The energy density control algorithm is a filtered-x LMS-based algorithm and takes the following form:

$$\begin{aligned}
w_i(n+1) = & w_i(n) - \mu \rho c v_x(n) r_{v_x}(n-i) \\
& - \mu \rho c v_y(n) r_{v_y}(n-i) - \mu \rho c v_z(n) r_{v_z}(n-i) \\
& - \mu p(n) r_p(n-i), \quad (30)
\end{aligned}$$

where $w_i(n)$ is the i th coefficient of the control filter at discrete time n , μ is a convergence parameter, v indicates the velocity components, r indicates the filtered reference signals, and $p(n)$ is the pressure at time n . For v , the subscripts x , y , and z indicate the direction of the velocity component, and for r , the subscripts indicate the signal being filtered (either pressure or the velocity components). This algorithm is based on updating the coefficients according to the negative gradient of the energy density. As such, it is only necessary to measure the pressure and velocity components and not the energy density itself. The squared pressure-control algorithm is also a filtered- x LMS-based algorithm and takes the form

$$w_i(n+1) = w_i(n) - \mu p(n) r_p(n-i). \quad (31)$$

Equations for multiple channel squared pressure and energy density control can be found in Ref. 9.

A transfer function must be estimated between the source and the pressure measurement as well as from the source to each of the three velocity measurements, for energy density control. For the squared pressure control, only the transfer function from the source to the pressure sensor is needed. The transfer functions were estimated passively and on-line using the techniques presented by Sommerfeldt and Tichy.¹⁰ The control algorithms were implemented using a Spectrum DSP96002 digital signal-processing card.

A schematic of the control system is shown in Fig. 1. In this experimental configuration, three control sensors and three control sources are employed. The noise excitation signal is used as a reference and is filtered by three adaptive filters, $W1(z)$ – $W3(z)$, to control the field produced by the noise source. For the squared pressure system, each sensor outputs a single time-domain pressure signal to the controller. For the energy density system, each sensor outputs six time-domain pressure signals to the controller. Two of these signals are used for each direction to estimate the velocity component, and the average of the six signals is used to estimate the pressure.

V. SQUARED PRESSURE AND ENERGY DENSITY FIELD NODES

The normalized squared pressure and normalized energy density fields for the (l,m,n) mode are described by

$$p_n^2(\mathbf{x}) = \cos^2 k_x x \cos^2 k_y y \cos^2 k_z z, \quad (32a)$$

$$\begin{aligned}
e_n(\mathbf{x}) = & \frac{1}{k^2} (k_x^2 \cos^2 k_y y \cos^2 k_z z + k_y^2 \cos^2 k_x x \cos^2 k_z z \\
& + k_z^2 \cos^2 k_x x \cos^2 k_y y). \quad (32b)
\end{aligned}$$

The locations of the nodes of these fields are determined by setting Eqs. (32) to zero. Therefore, the squared pressure field has nodes where $\cos k_x x$, $\cos k_y y$, or $\cos k_z z$ are zero. These nodes are located at

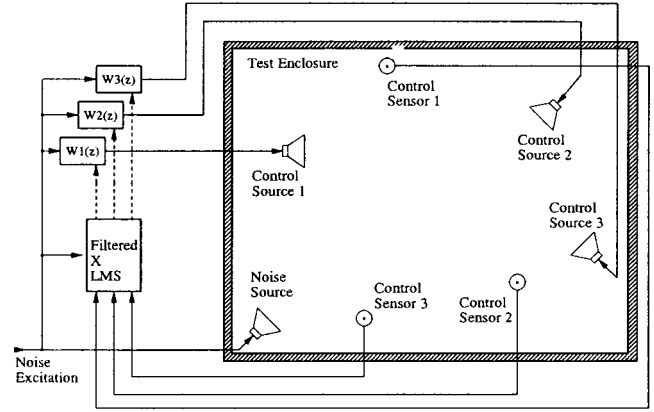


FIG. 1. Schematic of active control system.

$$\begin{aligned}
x &= \frac{\pi}{k_x} \left(\frac{2h+1}{2} \right), \quad 0 \leq x \leq L_x, \quad h=0,1,2,\dots, \\
y &= \frac{\pi}{k_y} \left(\frac{2i+1}{2} \right), \quad 0 \leq y \leq L_y, \quad i=0,1,2,\dots, \\
z &= \frac{\pi}{k_z} \left(\frac{2j+1}{2} \right), \quad 0 \leq z \leq L_z, \quad j=0,1,2,\dots,
\end{aligned} \quad (33)$$

which define nodal planes. There are l planes perpendicular to the x axis, m planes perpendicular to the y axis, and n planes perpendicular to the z axis for an (l,m,n) mode. Nodes for the energy density field, on the other hand, exist only when all three terms of Eq. (32b) are zero. This only occurs where the nodal planes of the squared pressure field intersect. Thus, the nodes of the energy density field exist as lines and there are no nodes in the energy density field for axial modes.

A volume velocity source, such as a loudspeaker, can generate a given mode if it is not located on a pressure node. Pressure sensors and energy density sensors can sense a given mode if they are not located on their respective nodes. Energy density sensors are statistically more likely to observe modes compared to pressure sensors, since the energy density field nodes are one-dimensional compared to the two-dimensional squared pressure-field nodes. Pressure fields composed of many modes will also have more regions of minima than energy density fields. A detailed discussion of energy density field nodes is presented in Ref. 11.

VI. THE TEST ENCLOSURE

The enclosure used for all the active control experiments measures $1.5 \times 2.4 \times 1.9$ m, and is shown in Fig. 2. Three Bose 101 speakers and one energy density sensor can be seen in this experimental configuration. The noise source speaker is mounted to the ceiling in the upper left corner of the enclosure, while two control source speakers are located on stands on the floor. The energy density sensor (the small light-colored sphere) can be seen on a microphone boom between the control sources. A scanning measurement system comprising slides, motors, cables, and a microphone array is also seen in the photograph.

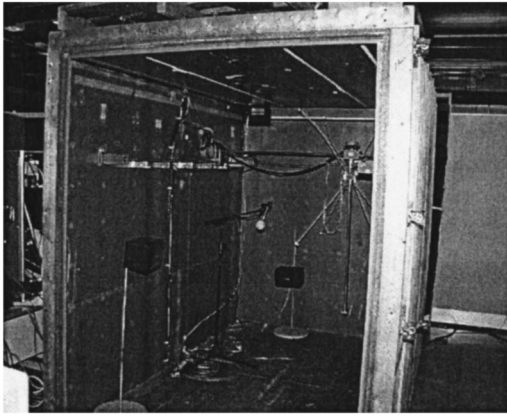


FIG. 2. Interior of enclosure used in active control experiments.

The walls of the enclosure consist of a $3\frac{3}{8}$ -in.-thick layer of sand sandwiched between a $\frac{3}{8}$ -in. chipboard layer (exterior surface) and a 2-in. particle-board layer (interior surface). Two-by-four bracing separates the particle board from the chipboard, and the sand fills the gap. The floor of the enclosure, which is isolated from the laboratory floor, does not have the sand or chipboard layers. The front wall of the enclosure is mounted on a structure with casters, and clamps into place. The enclosure has a very low transmission coefficient, and is therefore highly reverberant and relatively immune to external noise.

A simple method was used to determine the resonance frequencies of the enclosure. The enclosure was excited by bursts of random noise transmitted through the noise source. Measurements from a microphone located in the opposite corner were collected between excitations, and the spectra were averaged. The measurement therefore averaged energy due to the reverberant decay of the enclosure and not due to the forced signal. The reverberation power spectrum was normalized by the speaker response, and yielded the power spectrum shown in Fig. 3. The peaks in the power spectrum correspond to the resonances of the enclosure and are listed in Table I along with those predicted by theory. The predicted frequencies were calculated from Eq. (7). The difference between the experimental and predicted frequencies are also listed in Table I. All the measured resonances are shifted slightly higher than those predicted, which is likely due to finite vibrations of the walls.

Reverberation times of the enclosure were measured three times at three resonance frequencies: 73.25, 92.25, and 228.5 Hz, by measuring the time-domain energy decay slope. These resonance frequencies correspond to modes (0,1,0), (0, 0,1), and (2,0,0), respectively. The reverberation times are shown in Table II.

VII. COMPUTER MODEL

A computer program written in MATLAB™ was developed for this research to predict the results of active noise control in a rectangular enclosure. The program implements the equations of the previous sections using the approach developed by Nelson and Elliott,¹² with the optimal source strengths defined in Eqs. (12), (19), and (25).

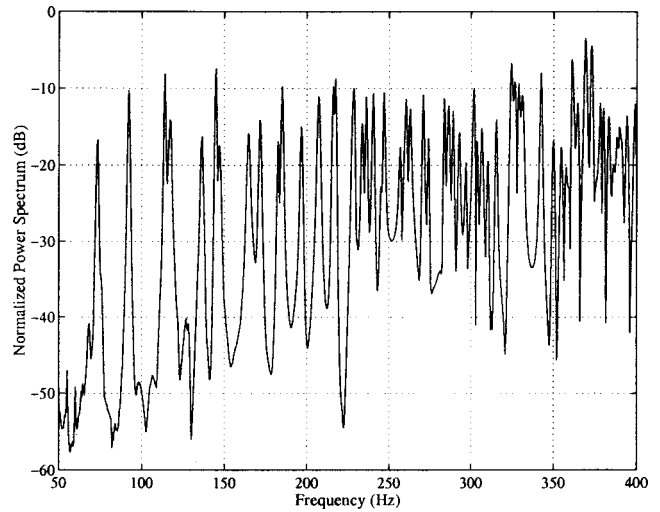


FIG. 3. Enclosure reverberation power spectrum, normalized by excitation speaker response.

The absorption coefficients of the enclosure walls were also required by the computer model. The absorption coefficients, α_{*} , are related to the mode indices, l , m , and n , and reverberation times, $T_{60,N}$, by the equation

$$\frac{\epsilon_l \alpha_x}{L_x} + \frac{\epsilon_m \alpha_y}{L_y} + \frac{\epsilon_n \alpha_z}{L_z} = \frac{55.28}{c T_{60,N}}. \quad (34)$$

The reverberation times measured for three modes yield three equations. The three equations were solved simultaneously for the absorption coefficients, and were determined to be $\alpha_x=0.0479$, $\alpha_y=0.0313$, and $\alpha_z=0.0730$. Each of these absorption coefficients is an average for a pair of opposing surfaces perpendicular to the indicated axis. The absorption coefficient for the floor and ceiling, $\alpha_z=0.0730$, was higher than that of the walls because the floor has much less mass than the walls, and therefore a higher transmission coefficient. Wall vibration was also taken into account, to some degree, in the program by modifying the enclosure dimensions as a function of frequency.⁹

It was determined experimentally that the sum of 80 modes accurately described the acoustic fields encountered. The contributions of the higher-order modes were minimal for the excitation frequencies used in the experiments. Thus, 80 modes were used in the numerical simulations. The 80 modes consisted of all mode combinations up to mode (3, 3, 4), consistent with the modal decomposition method described in the following section.

VIII. THE ACOUSTIC MEASUREMENT SYSTEM

The acoustic field measurement system acquires samples of the pressure within the enclosure at regular intervals in space. This is accomplished using an eight-channel microphone array seen in the right half of Fig. 2. The array is moved throughout the enclosure using three stepper motors and slides—one for each axis—controlled by a LABVIEW™ program. The use of the array allows samples to be collected at hard-to-reach locations, such as in the corners of the en-

TABLE I. Predicted and experimental resonance frequencies.

No.	Mode			Predicted frequency (Hz)	Experimental frequency (Hz)	Difference frequency (Hz)
	<i>l</i>	<i>m</i>	<i>n</i>			
1	0	0	0	0	NA	NA
2	0	1	0	71.82	73.25	1.43
3	0	0	1	90.64	92.25	1.61
4	1	0	0	113.50	114.00	0.50
5	0	1	1	115.65	117.25	1.60
6	1	1	0	134.31	136.25	1.94
7	0	2	0	143.63	144.75	1.12
8	1	0	1	145.25	147.00	1.75
9	1	1	1	162.04	164.5	2.46
10	0	2	1	169.85	171.75	1.90
11	0	0	2	181.29	182.75	1.46
12	1	2	0	183.07	185.00	1.93
13	0	1	2	195.50	196.50	1.50
14	1	2	1	204.28	207.00	2.72
15	1	0	2	213.89	216.00	2.11

closure. A ninth microphone is located in a corner of the test enclosure, in order to calculate transfer functions and complex pressures.

Low-resolution scanning samples the field throughout the enclosure, while high-resolution scanning samples the field only in the $z/L_z=0.21$ plane. There is a total of 576 low-resolution data acquisition points, forming an $8 \times 8 \times 9$ grid, where the grid spacings are $\Delta x=0.19$ m, $\Delta y=0.30$ m, and $\Delta z=0.21$ m. The high-resolution scan consists of 21×19 grid points, where the grid spacings are $\Delta x=0.071$ m and $\Delta y=0.119$ m. For single-frequency excitation of the enclosure, both the magnitude and phase of the pressures were recorded. For broadband excitation, the flat-weighted rms pressures were recorded. The low-resolution data were also used to determine the total potential energy in the enclosure using the equation

$$U_{\text{tot}} = \frac{1}{4\rho c^2} \sum_{i=1}^{576} |\hat{p}(\mathbf{x}_i)|^2. \quad (35)$$

The sample intervals are small enough for the low-resolution data that the pressure field data can be decomposed into their complex modal amplitudes. The N th axial mode spans N half-wavelengths in the enclosure. Therefore, the eighth axial mode in the x and y directions and the ninth axial mode in the z direction can be resolved, according to the Nyquist criterion. To be conservative, the modes were decomposed up to the third mode in the x and y directions, and the fourth mode in the z direction in these experiments. Thus, the worst case spatial sampling was 5.3 points per wavelength in the x and y directions, and 4.5 points per wavelength in the z direction. The highest mode resolved

TABLE II. Measured reverberation times for individual modes.

No.	Mode			Frequency (Hz)	T_{60} (s)
	<i>l</i>	<i>m</i>	<i>n</i>		
2	0	1	0	73.25	1.67
3	0	0	1	92.25	1.32
18	2	0	0	228.50	1.40

was the (3,3,4) mode, which corresponds to a frequency of over 540 Hz. The contributions of higher modes were low enough that antialiasing filters were not necessary when calculating the modal amplitudes.

The pressure fields were decomposed using the fact that the homogeneous wave equation within the enclosure forms a proper Sturm–Liouville system, and that the eigenfunctions are orthogonal.¹³ The pressure field, defined in Eq. (10), is multiplied by the eigenfunctions and integrated over the enclosure to yield the equation

$$Y = \int_0^{L_x} \int_0^{L_y} \int_0^{L_z} \sum_{N=1}^{\infty} \hat{C}_N \Psi_N(\mathbf{x}) \Psi_M(\mathbf{x}) dx dy dz. \quad (36)$$

The integral becomes zero when $M \neq N$, while the integral yields $\hat{C}_N V \Lambda_N$ if $M=N$. Therefore, the complex modal amplitudes can be found using the equation

$$\hat{C}_N = \frac{Y}{V \Lambda_N}, \quad (37)$$

where V is the enclosure volume. The complex pressure is only measured at discrete points; hence, the complex modal amplitudes are determined by using a discrete form of Eq. (36) to yield

$$\hat{C}_N = \frac{\Delta V}{V \Lambda_N} \sum_{i=1}^8 \sum_{j=1}^8 \sum_{k=1}^9 |\hat{p}(\mathbf{x}_{i,j,k})| (\cos \angle \hat{p}(\mathbf{x}_{i,j,k}) + j \sin \angle \hat{p}(\mathbf{x}_{i,j,k})) \Psi_N(\mathbf{x}_{i,j,k}), \quad (38)$$

where $\Delta V = \Delta x \Delta y \Delta z$, and $\angle \hat{p}(\mathbf{x}_{i,j,k})$ indicates the phase of the complex pressure signal. The complex pressure, $\hat{p}(\mathbf{x})$, is sampled and the eigenfunction, $\Psi_N(\mathbf{x})$, is evaluated at the point $\mathbf{x}_{i,j,k} = (x_i, y_j, z_k)$.

IX. PREDICTED AND EXPERIMENTAL ACTIVE CONTROL RESULTS

Various active control experiments were conducted in the course of this research. One broadband and three narrowband experiments are presented here. Single-frequency excitation was used in the narrowband experiments, while band-limited pink-noise excitation was used in the broadband experiment. The noise source excitation signals along with the dominant modes stimulated are listed in Table III. For the first two experiments, an excitation frequency near a resonance was used. In control configuration three, the room was excited at a frequency between resonances, and many modes were stimulated, while the enclosure was excited with band-limited pink noise in configuration four.

Up to three speakers distributed in the enclosure were used as control sources, while up to three control sensors were employed for each experiment. In each experiment, the same control source/sensor configuration was used for both the squared pressure and energy density control methods. The locations of the control sources and sensors are listed in Table III where the coordinates are normalized by the enclosure dimensions. The enclosure is defined in space by a corner at (0,0,0) and another at (1,1,1). A single loudspeaker serving as the noise source was always located at (0.12, 0.97, 0.97).

TABLE III. Predicted and experimental active control results.

No.	Control configuration			Predicted cancellation (dB)			Experimental cancellation (dB)	
	Excitation (mode)	Control sources	Control sensors	PE	SP	ED	SP	ED
1	171.5 Hz (0,2,1)	(0.05, 0.11, 0.04)	(0.34, 0.67, 0.24)	7.9	6.4	7.9	6.7	7.1
2	171.5 Hz (0,2,1)	(0.05, 0.11, 0.04) (0.34, 0.96, 0.04) (0.77, 0.97, 0.43)	(0.34, 0.67, 0.24) (0.68, 0.40, 0.49) (0.14, 0.15, 0.71)	16.1	-6.6	15.8	-2.5	14.4
3	130.0 Hz (many)	(0.05, 0.11, 0.04) (0.34, 0.96, 0.04) (0.77, 0.97, 0.43)	(0.34, 0.67, 0.24) (0.68, 0.40, 0.49) (0.14, 0.15, 0.71)	2.9	-4.8	1.5	-1.2	2.5
4	Pink noise	(0.05, 0.11, 0.04)	(0.32, 0.05, 0.50)	NA	NA	NA	1.8	3.8

The predicted and experimental cancellation results are also listed in Table III. The cancellation is defined as the difference in total potential energy between the uncontrolled and controlled fields, as determined from Eq. (35). Cancellation for the predicted and experimental squared-pressure control (SP) and energy density control (ED) are also listed in Table III. Only the predicted integrated potential energy density control (PE) cancellation is presented, since this control method cannot be implemented experimentally. The predicted integrated potential energy density control results are considered optimal, and are used as a baseline for comparing the other two control methods. Various data relating to these experiments are discussed below.

A. Single-frequency control

For the single-frequency excitation experiments, low-resolution and high-resolution data were collected. The low-resolution data were used to determine the total potential energy in the enclosure, as well as to calculate the complex modal amplitudes, \hat{C}_N , of the decomposed pressure fields. For each experiment, the magnitudes of the first 40 modes are plotted for the predicted and experimental results using the equation

$$\text{Magnitude (dB)} = 20 \log |\hat{C}_N|. \quad (39)$$

Predicted results comprise the integrated potential energy density, squared pressure, energy density, and uncontrolled cases. The magnitudes of the experimentally determined complex modal amplitudes are plotted below the predicted results. High-resolution sound-pressure-level data in the $z/L_z=0.21$ plane are plotted in the figures, following the modal magnitude data for each experiment. The sound-pressure level L_p is found from

$$L_p \text{ (dB)} = 20 \log(p_{\text{rms}}/p_{\text{ref}}), \quad (40)$$

where p_{rms} is the measured pressure and $p_{\text{ref}}=20 \mu\text{Pa}$. Again, predicted results are plotted at the top half of the figure, with the experimental results presented in subfigures below them.

1. 171.5-Hz on-resonance control

Two experiments are presented where 171.5 Hz was the excitation frequency. In general, the experimental results for

these two control configurations, seen in Figs. 4–7, are consistent with the predictions. The magnitudes of the complex modal amplitudes match fairly well for the dominant modes, while the predicted and experimental pressure fields have similar contours. The cancellation performance achieved experimentally is also consistent with the predictions, as seen in Table III.

In Figs. 4(a) and 4(e), 6(a) and 6(e), the magnitudes of the modes of the predicted and experimental uncontrolled pressure fields are plotted. The excitation frequency is very close to the resonance frequency of 171.75 Hz, corresponding to the tenth mode (0,2,1). The tenth mode is dominant in the two plots, followed by the ninth mode (1,1,1). The magnitudes of the tenth and ninth modes are consistent between those predicted and measured, though two mode magnitudes vary considerably between the predicted and measured results. The experimental results show the fifth and 20th modes to have substantially higher amplitudes than the prediction, which may be due to finite wall vibration.

It was expected that control configuration 1 would yield only fair cancellation for both the energy density and squared pressure control, since the control source is not in a desirable location. Either the ninth or tenth mode produced by the control source will be out of phase with the modes produced by the noise source, but not both. The control sensor, on the other hand, is located in a desirable position. It can observe both the ninth and tenth modes since it is not located near pressure or energy density nodes for these two modes. The pressure-field nodal planes for the tenth mode are located at $y/L_y=0.25$, $y/L_y=0.75$, and $z/L_z=0.5$, while the pressure field nodal planes for the ninth mode are located at $x/L_x=0.5$, $y/L_y=0.5$, and $z/L_z=0.5$. The energy density nodal lines are located at the intersections of these planes.

The predicted and experimental mode magnitudes for configuration 1 generally follow the same trends for the squared pressure and energy density control methods shown in Fig. 4. The mode magnitudes for the energy density control are also very close to those predicted for the optimal control. The pressure fields shown in Fig. 5 are quite consistent between the predicted and experimental results. The predicted and experimental results for the energy density control method are also very similar to the optimal solution, indicating that the energy density control solution yielded nearly the

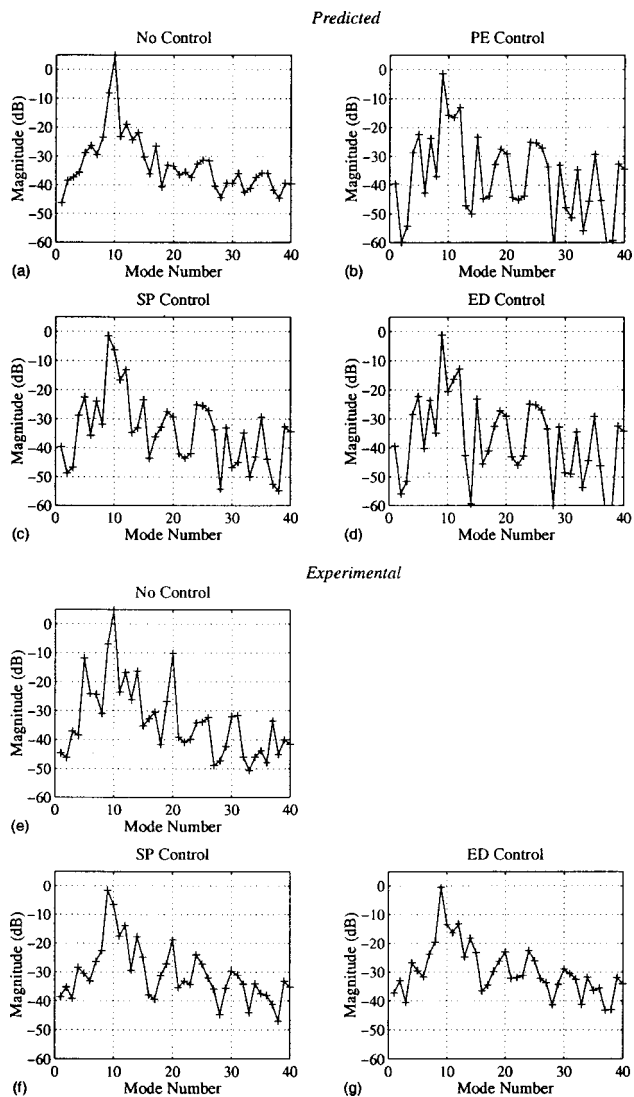


FIG. 4. Control configuration 1. Predicted and experimental mode magnitudes. 171.5 Hz, mode (0,2,1) excitation.

optimal control. Cancellation predictions, in Table III, are within 0.8 dB for both measured control methods.

Three control sources and three error sensors were used in configuration 2, while the excitation frequency was again 171.75 Hz. The second control sensor is located very close to the ninth and tenth mode pressure-field nodes. Thus, this sensor is not effective at sensing these two modes in the pressure field. The third sensor is located at a good position for both the energy density and pressure fields. The second control source is located at a desirable location since it is able to produce both the tenth and ninth modes out of phase with the noise source. The third source is located near the pressure node $z/L_z=0.5$, and therefore will tend to produce a field with minimal contribution from the ninth and tenth modes. Therefore, this source will be ineffective at controlling the ninth or tenth modes.

It can be seen in Table III and Figs. 6 and 7 that the squared pressure control increases the total potential energy in the enclosure, while the energy density control achieves significant cancellation. In both the predicted and experimental squared pressure-control mode amplitude results, seen in

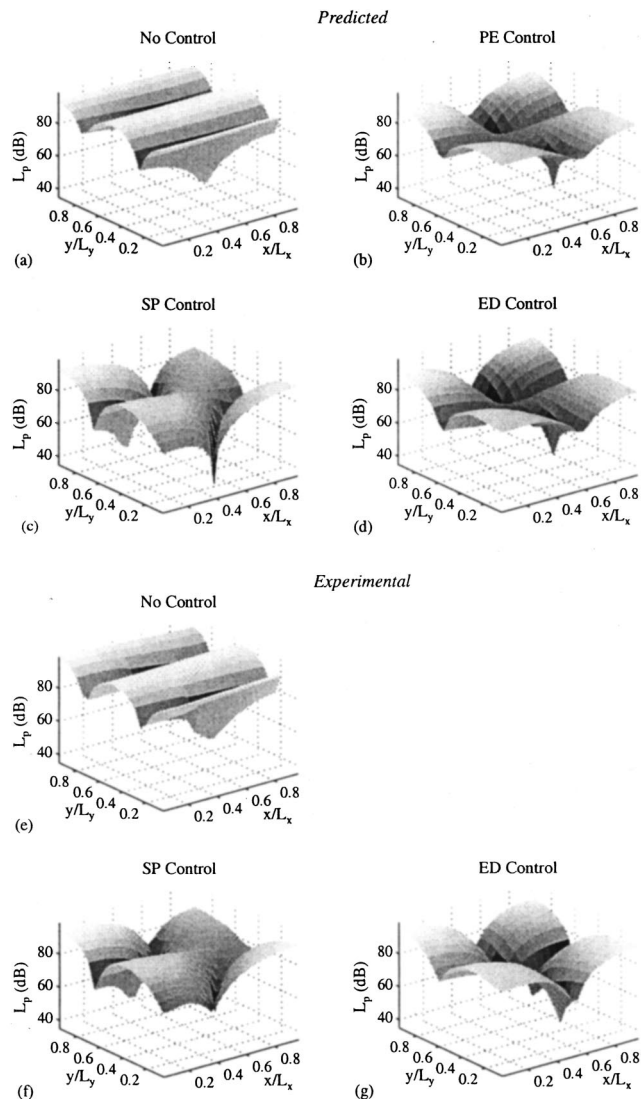


FIG. 5. Control configuration 1. Predicted and experimental sound-pressure distributions for the $z/L_z=0.21$ plane. 171.5 Hz, mode (0,2,1) excitation.

Figs. 6(c) and 6(f), the ninth and tenth modes have equal amplitude. The magnitude of the ninth mode has significantly increased, causing an increase in the overall potential energy in the enclosure. On the other hand, the ninth and tenth modes have been significantly reduced for the case of energy density control, seen in Figs. 6(d) and 6(g) and there is no dominant mode as a result. The pressure-field contours for the energy density control, seen in Figs. 7(d) and 6(g), are therefore fairly complicated, though there is still some general agreement between the predicted and experimental results. The energy density control results match the optimal control results more closely than the squared pressure results in general for this configuration.

2. Off-resonance control

In configuration 3, three sources and sensors are used to control a field generated by a 130-Hz tone. Controlling fields generated by frequencies between resonances—as in configuration 3—is difficult, due to the control source(s) inability to create the complex pressure field produced by the noise

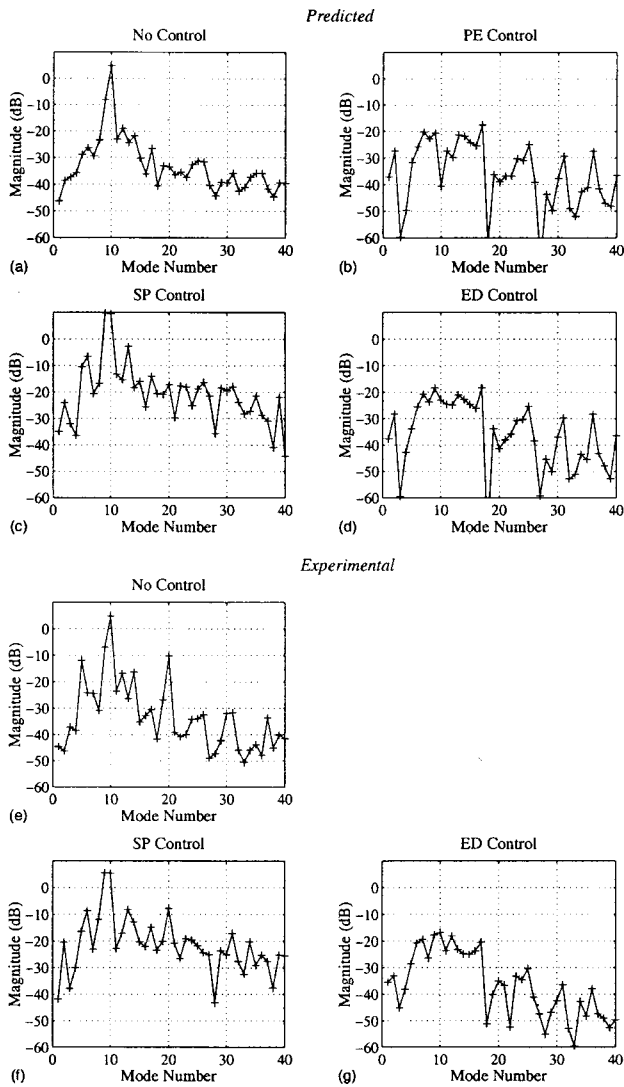


FIG. 6. Control configuration 2. Predicted and experimental mode magnitudes. 171.5 Hz, mode (0,2,1) excitation.

source. Many modes must be generated with the correct phase relationships when controlling these fields. The excitation frequency is between the fifth mode (0,1,1) frequency at 117.25 Hz and the sixth mode (1,1,0) frequency at 136.25 Hz. Hence, nearby modes are excited by the noise source. The fifth, sixth, eighth, and ninth modes are all within 10 dB of each other, and are the dominant modes seen in Fig. 8(a) for the uncontrolled field.

Though many modes contribute to the fields encountered in this configuration, the results show the same trends. The predicted and experimental cancellation for the squared pressure and energy density control, shown in Table III, both indicate the squared pressure control increasing the total potential energy in the enclosure, while the energy density control reduces the total potential energy. The results for the measured uncontrolled field and the energy density controlled field are consistent with those predicted in Figs. 9(a) 9(d), 9(e), and 9(g), though the measured energy density field is offset in overall magnitude in the pressure-field plot. In this configuration, neither the squared pressure nor the energy density control yields the optimal solution, though the energy density control mode magnitudes more closely re-

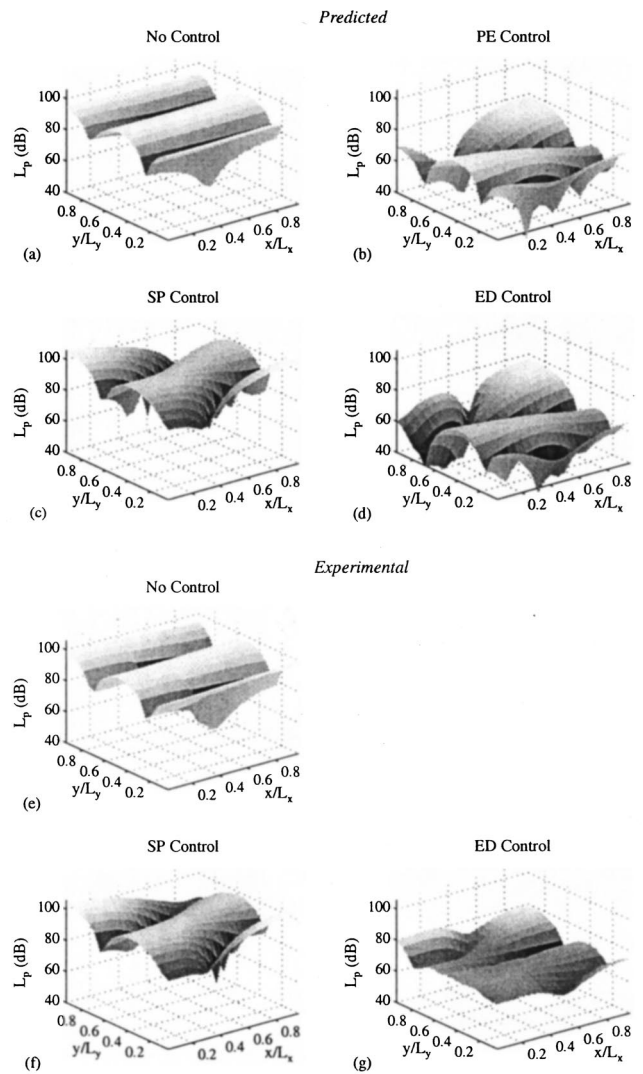


FIG. 7. Control configuration 2. Predicted and experimental sound-pressure distributions for the $z/L_z=0.21$ plane. 171.5 Hz, mode (0,2,1) excitation.

semble the optimal control mode magnitude results. The squared pressure-controlled fields, in Figs. 9(c) and 9(f) and mode magnitude plots, in Figs. 8(c) and 8(f) also show similar trends. Even though this control configuration was relatively complex, due to off-resonance excitation and multiple source/sensors, the computer model was able to predict the results with reasonable accuracy.

B. Broadband control

A single broadband control experiment, configuration 4, is presented here. Pink noise was filtered through a fourth-order 100-Hz Butterworth low-pass filter for excitation of the enclosure. A single control source and a single control sensor were used. The control sensor was positioned closer to the control source than to the noise source, since the control algorithm needs time to filter the reference signal. This delay plus the delay from the control source to the sensor must be less than the delay from the noise source to the sensor, or else the control signal will lag behind the signal to be canceled.^{13,14}

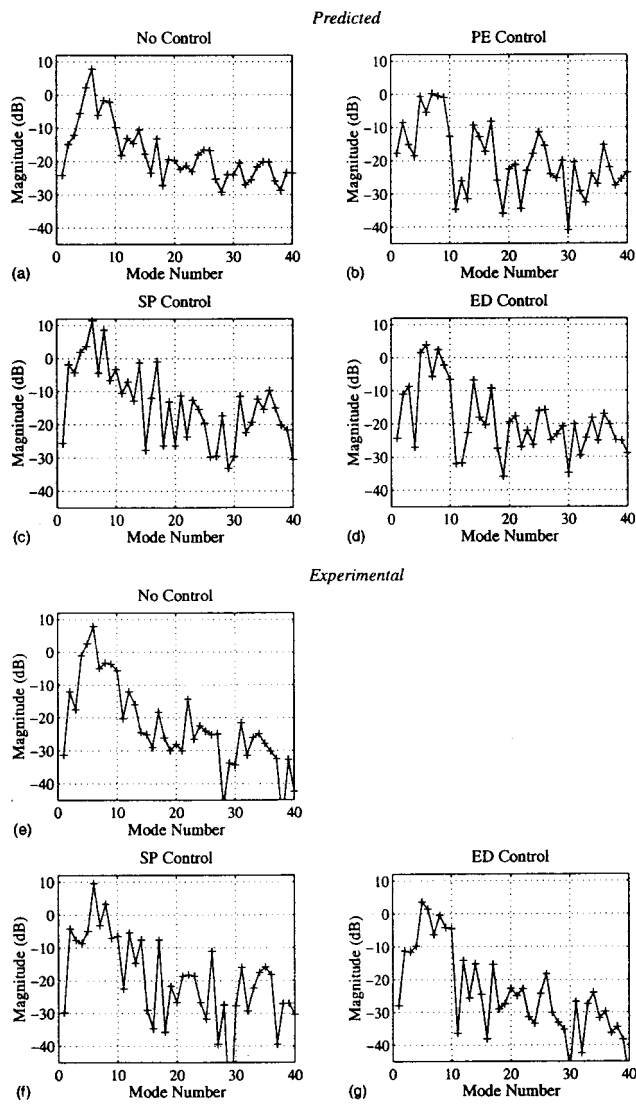


FIG. 8. Control configuration 3. Predicted and experimental mode magnitudes. 130 Hz, off-resonance excitation.

The low-resolution data were used to calculate the total potential energy in the enclosure, by measuring the rms sound-pressure level at each sample point. The sound fields were not decomposed into their modes since complex pressure data, at each point in space, were not measured for the random excitation. (A transfer function would have been required for each point in space to perform modal decomposition, and would have resulted in 576 transfer functions to process for each field.) High-resolution sound-pressure-level data in the $z/L_z=0.21$ plane were collected and are presented in Fig. 10. Power spectra at the control sensor and at a reference microphone in a corner of the enclosure are presented in Figs. 11 and 12 for the uncontrolled and controlled fields. No simulations were run to predict the performance of the broadband control.

The sensor, located at $(0.32, 0.05, 0.50)$, will not observe modes having a pressure node at $z/L_z=0.50$, when using squared pressure control. These modes are mode three (92.25 Hz), mode five (117.25 Hz), mode eight (147 Hz), mode nine (164.5 Hz), and so on. Hence, the control performance at these frequencies is unpredictable for the squared pressure-

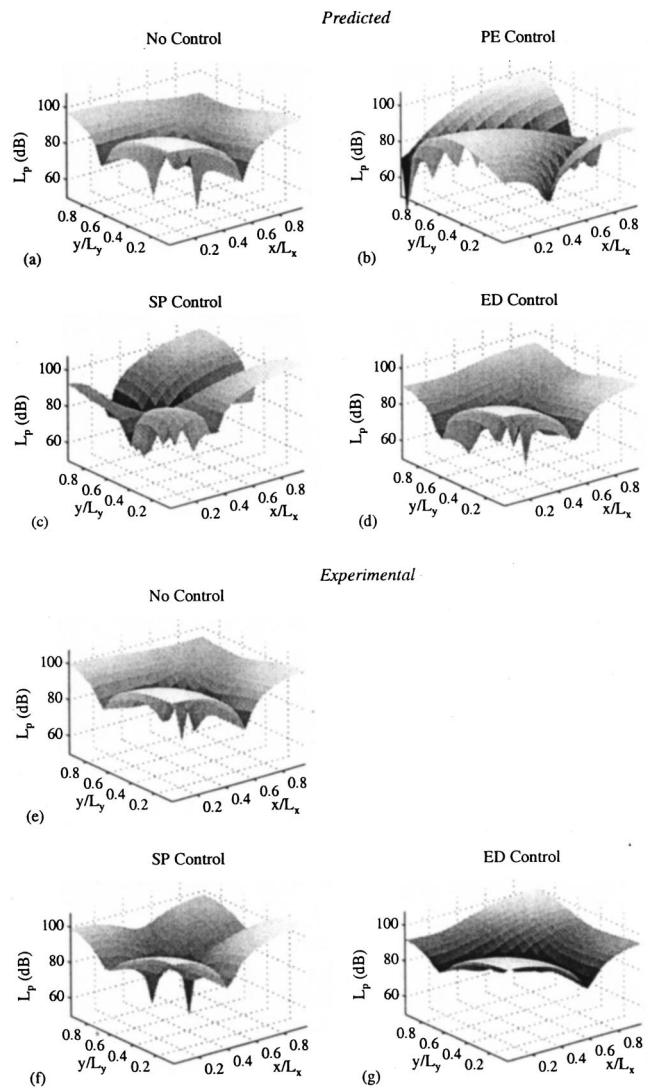


FIG. 9. Control configuration 3. Predicted and experimental sound-pressure distributions for the $z/L_z=0.21$ plane. 130 Hz, off-resonance excitation.

control method. The control source, located at $(0.05, 0.11, 0.04)$, is near a corner of the enclosure and is in a generally desirable position.

The pressure field for the energy density control method is lower overall compared to the pressure field for the squared pressure-control method, shown in Fig. 10. This is reflected in the measured reduction in total potential energy, where the energy density control method yielded 3.8 dB of cancellation while the squared pressure-control method yielded 1.8 dB. The shapes of the controlled pressure fields are similar in shape and no longer have the $(0,1,0)$ mode contour of the uncontrolled field.

In Fig. 11, it can be seen that the measurement microphone, which is at the sensor location, is virtually not observing the pressure from the 92.25-Hz energy in the field. This is due to the associated mode of this frequency having a pressure node at the sensor location. The two control methods yield cancellation spectra that are similar, yet with an important difference. Both the squared pressure and energy density control methods reduce the power spectra in the frequency regions around mode two, mode four, and mode five,

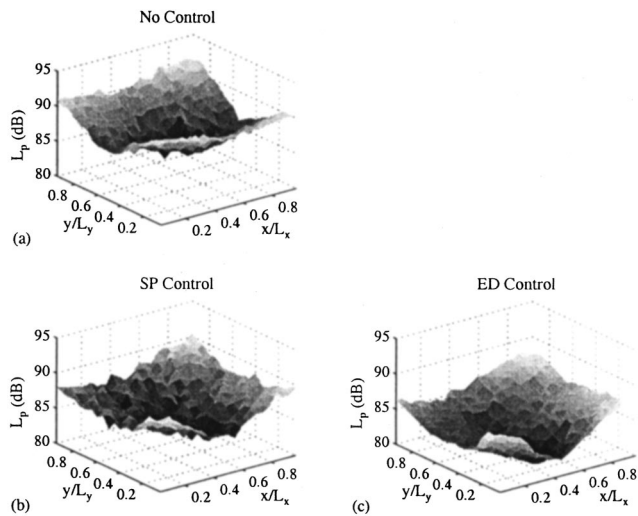


FIG. 10. Control configuration 4. Experimental sound-pressure distributions for the $z/L_z=0.21$ plane. Pink noise excitation.

and both the control methods are ineffective above approximately 125 Hz. On the other hand, there is a dip in the spectrum for the energy density control method at 92.25 Hz not seen in the squared pressure-control plot.

Though the microphone at the sensor did not measure substantial energy at 92.25 Hz, the reference microphone observes all modes in the enclosure, and a peak is seen at this frequency in Fig. 12 for the uncontrolled field. The response is also seen to have increased at 117.25, 147, and 164.5 Hz. In Fig. 12, it is easier to see that the energy density control method is reducing the energy in the enclosure at 92.25 Hz, while the squared pressure-control method is ineffective. Greater cancellation is also achieved at 117.25 Hz and 136.25 Hz for the energy density control method compared to the squared pressure-control method, though the performance is slightly worse around 147 Hz. Due to the greater ability of the error sensor to observe modes, the energy density control method is superior to the squared pressure-control method for this broadband excitation experiment.

X. CONCLUSIONS

The goal of this research was to investigate the efficacy of an active control system based on minimizing the sum of the total energy densities at discrete points in space for reducing the acoustic pressure field in a three-dimensional enclosure. To achieve this end, a numerical model was used to predict, and a physical system was constructed to measure, the performance of this active control system. The optimal solution for the energy density control method was determined for use in a computer program. To gauge its benefits, the total energy density control system was compared to the relatively common active control system based on minimizing the sum of the squared pressures at points in space. The squared pressure-control system was also modeled numerically and implemented physically. Both systems were compared to the predicted results of minimizing the integrated potential energy density, which is considered the optimal control method. A measurement system was also constructed

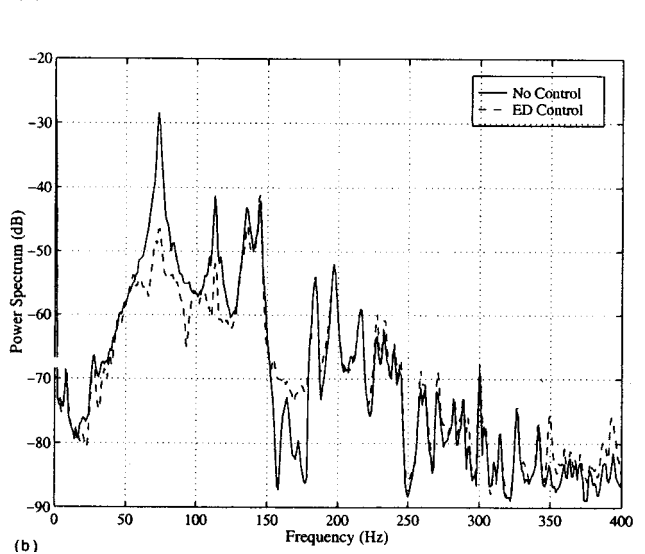
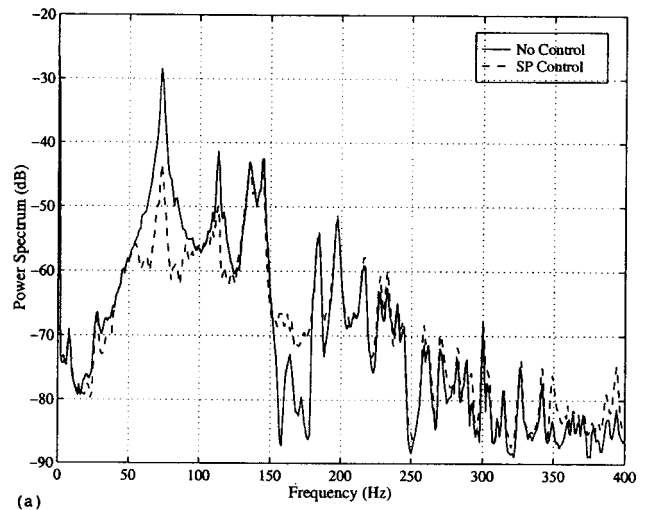
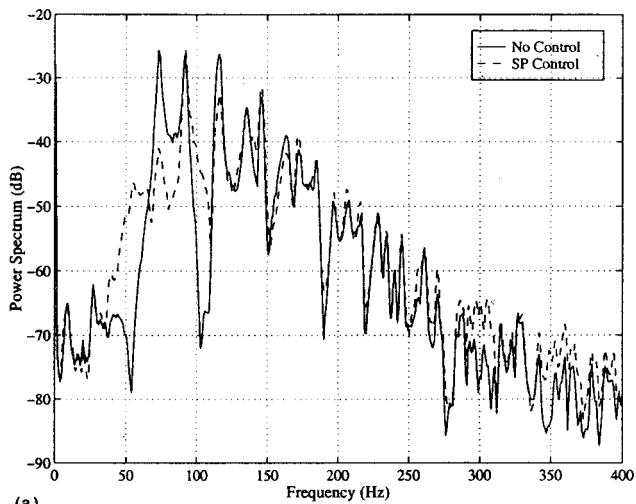


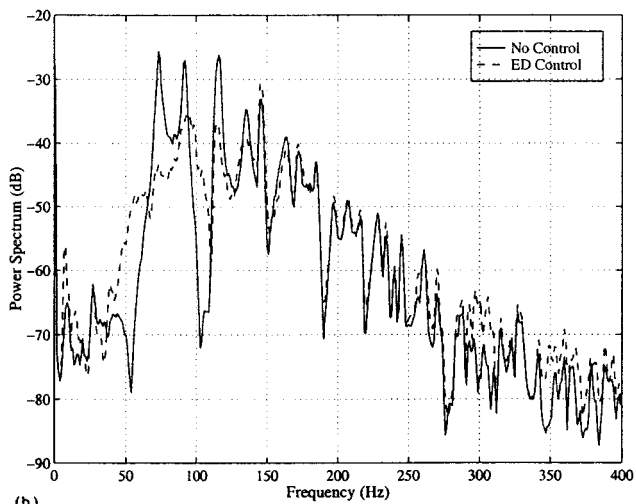
FIG. 11. Control configuration 4. Power spectra (*re* $1 \text{ V}^2/\text{Hz}$) measured at control sensor for no control and broadband active control. (a) Squared pressure control. (b) Energy density control.

that could be used to characterize the performance of active control systems in an enclosure through modal decomposition.

Energy density control was superior to the squared pressure control in both narrowband and broadband experiments due to its ability to better sense the acoustic modes. Nodes exist as planes for squared pressure modes, while nodes exist as lines for energy density modes. It is less likely for error sensors to be located at energy density field nodes than squared pressure nodes; hence, fewer sensors are required for the energy density control method to achieve results comparable to that of the squared pressure method. Up to 14.4 and 3.8 dB of cancellation were achieved for the energy density control method for narrowband and broadband experiments, respectively. The close agreement between predicted and experimental results indicates that the energy density sensor, developed in the companion paper,⁸ has sufficient accuracy for use in active noise control. The close agreement between predicted and experimental results also shows that an active control system based on the energy density can successfully be constructed.



(a)



(b)

FIG. 12. Control configuration 4. Power spectra ($re 1 V^2/Hz$) measured at reference microphone for no control and broadband active control. (a) Squared pressure control. (b) Energy density control.

The energy density control method used in this research requires the three components of particle velocity as well as the pressure for each error sensor. Thus, a single energy density sensor required four times the signal processing compared to a single pressure sensor. In previous research involving a statistical analysis, it was predicted that an energy-density-based active control system would require approximately one-fourth the number of sensors compared to the squared pressure method (depending on the modal composition of the pressure field) for comparable performance.¹¹

Thus, the energy density control approach used here is comparable in performance to a squared pressure-control system of similar signal-processing complexity. A benefit of the energy density approach is that compact energy density sensors can be employed, whereas approximately four times the number of pressure sensors must be distributed within the control space, requiring significantly more cabling. In the future, combining the pressure and three velocity measurements into a single energy density measurement might prove to be advantageous. A single channel for processing would then be required per sensor, as in the squared pressure control, instead of four channels.

ACKNOWLEDGMENTS

The authors would like to thank the Applied Research Laboratory at Penn State University and NASA Langley for their support of this research.

- ¹S. J. Elliot, P. A. Nelson, I. M. Stothers, and C. C. Boucher, "In-Flight Experiments on the Active Control of Propeller-Induced Cabin Noise," *J. Sound Vib.* **140**, 219–238 (1990).
- ²S. D. Sommerfeldt and P. J. Nashif, "Energy Based Control of the Sound Field in Enclosures," *Second International Congress on Recent Developments in Air and Structure-Borne Sound and Vibration*, pp. 361–368 (March, 1992).
- ³S. D. Sommerfeldt, J. W. Parkins, and Y. C. Park, "Global Active Noise Control in Rectangular Enclosures," *Proc. ACTIVE 95*, pp. 477–488 (1995).
- ⁴Y. C. Park and S. D. Sommerfeldt, "Global Attenuation of Broadband Noise Fields Using Energy Density Control," *J. Acoust. Soc. Am.* **101**, 350–359 (1997).
- ⁵X. Qui, C. H. Hansen, and X. Li, "A Comparison of Near-Field Acoustic Error Sensing Strategies for the Active Control of Harmonic Free Field Sound Radiation," *J. Sound Vib.* **215**, 81–103 (1998).
- ⁶P. A. Nelson, A. R. D. Curtis, S. J. Elliot, and A. J. Bullmore, "The Active Minimization of Harmonic Enclosed Sound Fields," *J. Sound Vib.* **117**, 1–58 (1987).
- ⁷F. J. Fahy, *Sound Intensity* (Spon, London, 1995), pp. 91–97.
- ⁸J. W. Parkins, S. D. Sommerfeldt, and J. Tichy, "Error Analysis of a Practical Energy Density Sensor," *J. Acoust. Soc. Am.* **108**, 211–222 (2000).
- ⁹J. W. Parkins, "Active Minimization of Energy Density in a Three-Dimensional Enclosure," Ph.D. thesis, Pennsylvania State University, University Park, PA (1998), pp. 101–104.
- ¹⁰S. D. Sommerfeldt and J. Tichy, "Adaptive Control of a Two-Stage Vibration Isolation Mount," *J. Acoust. Soc. Am.* **88**, 938–944 (1990).
- ¹¹J. W. Parkins, J. Tichy, and S. D. Sommerfeldt, "A Comparison of Two Active Control Methods Through an Investigation of Node Structures," *Proc. ACTIVE 99*, pp. 729–740 (1999).
- ¹²P. A. Nelson and S. J. Elliott, *Active Control of Sound* (Academic, San Diego, 1993), pp. 314–329.
- ¹³E. Kreyszig, *Advanced Engineering Mathematics: Sixth Edition* (Wiley, New York, 1988), pp. 225–228.
- ¹⁴D. Guicking and M. Bronzel, "Multichannel Broadband Active Noise Control in Small Enclosures," *Proc. Inter-Noise 90*, Vol. 2, pp. 1255–1258 (1990).